ADVANCED FUNCTIONAL MATERIALS
www.afm-journal.de

Solid State Reaction Epitaxy, A New Approach for Synthesizing Van der Waals heterolayers: The Case of Mn and Cr on Bi_2Se_3

*Salma Khatun, Onyedikachi Alanwoko, Vimukthi Pathirage, Caique C. de Oliveira, Raphael M. Tromer, Pedro A. S. Autreto, Douglas S. Galvao, and Matthias Batzill**

Van der Waals (vdW) heterostructures that pair materials with diverse properties enable various quantum phenomena. However, the direct growth of vdW heterostructures is challenging. Modification of the surface layer of quantum materials to introduce new properties is an alternative process akin to solid state reaction. Here, vapor deposited transition metals (TMs), Cr and Mn, are reacted with Bi_2Se_3 with the goal to transform the surface layer to XBi_2Se_4 (X = Cr, Mn). Experiments and ab initio MD simulations demonstrate that the TMs have a high selenium affinity driving Se diffusion toward the TM. For monolayer Cr, the surface Bi_2Se_3 is reduced to Bi_2-layer and a stable (pseudo) 2D $Cr_{1+\delta}Se_2$ layer is formed. In contrast, monolayer Mn can transform upon mild annealing into $MnBi_2Se_4$. This phase only forms for a precise amount of initial Mn deposition. Sub-monolayer amounts dissolve into the bulk, and multilayers form stable MnSe adlayers. This study highlights the delicate energy balance between adlayers and desired surface modified layers that governs the interface reactions and that the formation of stable adlayers can prevent the reaction with the substrate. The success of obtaining $MnBi_2Se_4$ points toward an approach for the engineering of other multicomponent vdW materials by surface reactions.

1. Introduction

Interface reactions between solids have been extensively utilized to fabricate materials that are otherwise difficult to synthesize and have found applications from battery materials[1–3] to superconductors.[4,5] Generally, the driving force for such reactions is the chemical potential driven diffusion of elements from one compound to another to form materials with lower formation energy.[6] The interest in van der Waals (vdW) materials for enabling new quantum phenomena may require applications of such technologies also for modifying this class of materials. Here we investigate the transformation of surfaces of vdW materials by reacting with ultrathin adlayers is a potential approach for creating new or modified 2D materials. However, in contrast to traditional solid state reactions, these reactions may occur only with precisely controlled adlayers. It can be envisioned, that such a technology can also exploit the planar nature of the materials and exert local control by using shadow masking to "emboss" patterns in extended van der Waals sheets. The nature of 2D materials with their structurally confinement in two dimensions and the lack of covalent bonds to a substrate, is expected to make structural transformations by solid state reactions feasible without interface restructuring. Lower temperatures compared to traditional solid-state reactions are anticipated if the reaction is reduced to the nanoscale by only converting a single molecular 2D sheet. Thus, modifications by solid state reactions may offer new perspectives and opportunities for vdW materials design.

We study the reaction of Bi_2Se_3 with Mn or Cr with the aim to synthesize XBi_2Se_4 (X = Mn or Cr) on top of a bulk Bi_2Se_3 substrate as an example for surface reactions in vdW systems. $MnBi_2Se_4$ is a known compound that may be synthesized as bulk crystals or as thin films by molecular beam epitaxy.[7,8] In contrast, $CrBi_2Se_4$ has only been considered theoretically[9,10] but not yet realized. These studies are motivated by the modification of topological insulators with magnetic materials. Pairing of magnetic properties with topological insulator states will break the time-reversal symmetry (TRS) and several exotic phenomena like the quantum anomalous Hall (QAH) effect, axion insulator state, quantized magnetoelectric effect, or Majorana fermions, are expected in these materials.[11,12] Introduction of magnetic properties in TI was first attempted by dilute doping,[13,14] however, the observation of breaking of

S. Khatun, O. Alanwoko, V. Pathirage, M. Batzill
Department of Physics
University of South Florida
Tampa, FL 33620, USA
E-mail: mbatzill@usf.edu
C. C. de Oliveira, P. A. S. Autreto
Federal University of ABC (UFABC)
Santo Andre-SP 09040-902, Brazil
R. M. Tromer, D. S. Galvao
State University of Campinas
Campinas-SP 13083-959, Brazil
The ORCID identification number(s) for the author(s) of this article can be found under https://doi.org/10.1002/adfm.202315112

DOI: 10.1002/adfm.202315112

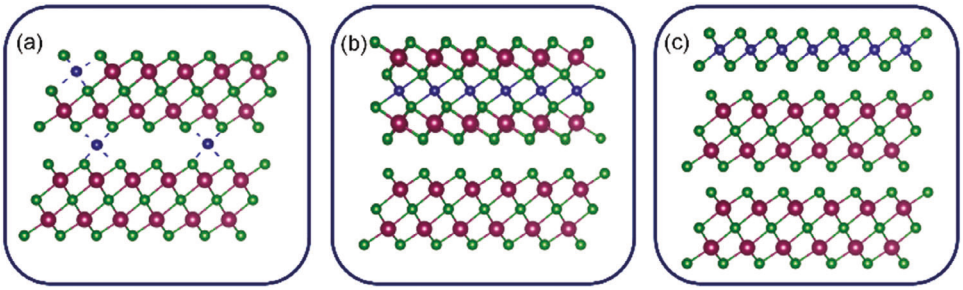

Figure 1. Schematic illustration of the different possibilities of inclusion of magnetic dopants (Cr or Mn) inside Bi_2Se_3 crystal. a) The first possibility is to either substitute Bi or intercalate between the QLs. b) The second possibility is to reside within the QL and form a mixed septuple layer ($CrBi_2Se_4$ or $MnBi_2Se_4$). c) The third possibility is to grow a heterostructure with a sharp interface. (We have drawn here a transition metal dichalcogenide structure for simplicity).

TRS in these materials has been controversial.[15] Formation of magnetic/TI vdW-heterostructure[16–18] has been suggested as an alternative approach, and thus the synthesis of magnetic $MnBi_2Se_4$ or $CrBi_2Se_4$ vdW layers on top of the topological insulator Bi_2Se_3 makes this a promising system. Because of these applications, the synthesis of $MnBi_2Se_4$ has been studied by MBE in thin films and for bulk materials.[7,8,19] The demonstrated stability and favorable formation of $MnBi_2Se_4$ makes it also an interesting candidate to explore the solid-state reaction of Mn with Bi_2Se_3. By comparing it with Cr, we can identify driving forces for such reactions, which helps us to gain insight into the reaction mechanisms and gauge the potential and limitations of this solid-state transformation process in vdW systems.

Our results demonstrate the possibility of transforming vdW materials by solid state reactions and thus the synthesis of vdW heterostructures by surface reactions, which we term "solid state reaction epitaxy". In contrast to traditional epitaxy, where a film is grown on a substrate, here the substrate (or more precisely the surface-layer of the substrate) is being transformed into a new material and thus the substrate is being consumed in a reaction to form the new desired material. A detailed analysis shows that for Mn this approach works for a narrow regime of temperature and deposited Mn reacts with Bi_2Se_3 to obtain $MnBi_2Se_4$. For too small amounts, Mn diffuses into the bulk while larger amounts favor the formation of MnSe adlayers by reaction with Se diffusing from Bi_2Se_3. This is similar to Cr, which prefers the formation of Cr-selenide adlayer (a pseudo 2D material) by reaction with Se rather than the formation of $CrBi_2Se_4$. The successful formation of $MnBi_2Se_4$ but failing to form $CrBi_2Se_4$ by solid state reaction is explained by a combination of the favorable stability of $MnBi_2Se_4$ compared to $CrBi_2Se_4$, but also the higher stability of $Cr_{1+\delta}Se_2$ compared to MnSe monolayers. In other words, deposited Cr reacts with Se to a Cr-selenide adlayer while a Mn-selenide add layer is less stable and thus $MnBi_2Se_4$ can be obtained. Ab initio molecular dynamics simulations support the experimental results and show a stronger affinity of Se to Cr, compared to Mn, but also demonstrate that both TM extract Se from Bi_2Se_3. All the results together, illustrate that the formation energies of all different phases need to be considered especially if other low energy (pseudo)2D phases like $Cr_{1+\delta}Se_2$ can form that compete with the desired reaction to obtain XBi_2Se_4.

2. Results and Discussion

There are a few possibilities in which Cr or Mn can react with Bi_2Se_3 quintuple layers (QLs) illustrated in **Figure 1**. The first possibility is for Cr/Mn to substitute Bi and (or) intercalate inside the van der Waals gap between two QLs (Figure 1a). The second possibility is to reside in the QL and form the desired ordered $CrBi_2Se_4/MnBi_2Se_4$ septuple layer alloy (Figure 1b). The third possibility is to create a sharp heterostructure with transition metal chalcogenides on top (Figure 1c). As we will show below, the different Se concentrations in these surface layers can be compensated for by Se diffusion from the bulk crystal.

To form a $TMBi_2Se_4$ septuple layer, we deposited a monolayer amount of transition metal (TM) on the Bi_2Se_3 surface at room temperature (RT) and subsequently vacuum annealed at 200 °C, 250 °C, and 300 °C. To understand the atomic arrangement of the elements in the surface layer, we have used He^+ low energy ion scattering spectroscopy (LEIS), an extremely surface-sensitive technique generally used to probe the elemental composition of the topmost surface atoms.[20] Thus, we may distinguish if Cr/Mn remains in the surface layer or diffuse to the subsurface to form $CrBi_2Se_4/MnBi_2Se_4$. In addition to LEIS, we have employed X-ray photoemission spectroscopy (XPS) to determine the compositional and chemical-state changes in different stages of surface reaction. Scanning tunneling microscopy (STM) has been used to get detailed information on the morphology during the transformation processes. The extraction of Se by deposited TM from Bi_2Se_3 and the formation of TM-chalcogenides has also been studied by ab initio molecular dynamics (AIMD). In a separate experiment, we codeposited the metals (Mn or Cr) and chalcogen (Se)- akin to MBE-in order to evaluate the role of extraction of Se from the Bi_2Se_3 by the TM plays for the reaction of TM with Bi_2Se_3.

2.1. Low Energy Ion Scattering Spectroscopy

Figure 2a shows the LEIS spectrum of pristine Bi_2Se_3 acquired with 1200 eV He^+ ions. He ions scattered from the lighter Se atoms are detected at ≈975 eV, and He-ions scattered from the heavy Bi atoms are detected at ≈ 1060 eV. Figure 2b shows LEIS spectra for a monolayer amount of Cr deposited on Bi_2Se_3 at room temperature (RT) and subsequently annealed at 200 °C, 250 °C, and 300 °C. After room temperature deposition, an

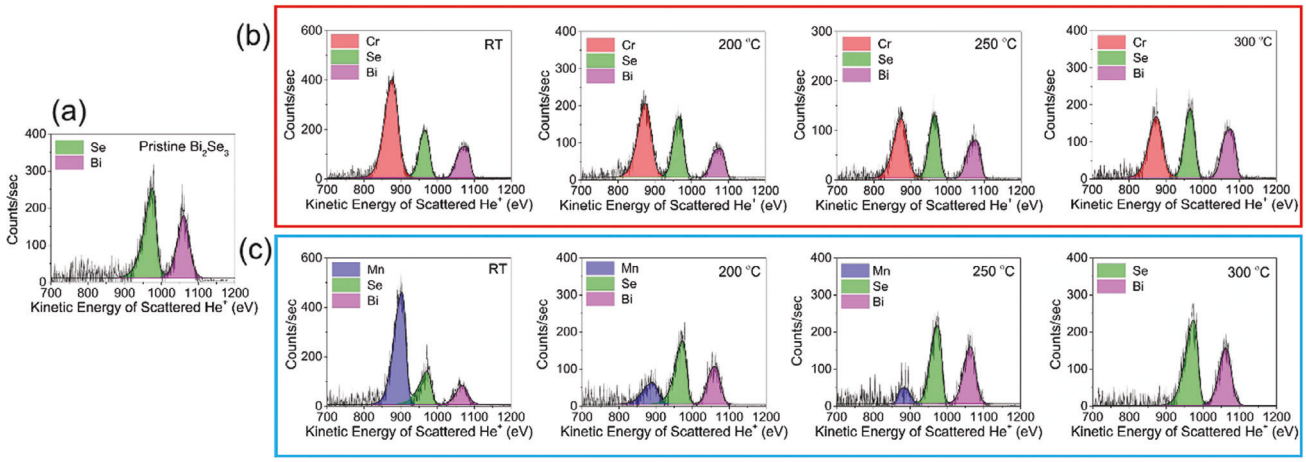

Figure 2. LEIS analysis of reaction epitaxy of Cr or Mn with Bi_2Se_3 single crystal. a) LEIS spectrum of Bi_2Se_3. LEIS spectra of monolayer amount of b) Cr or c) Mn deposited on Bi_2Se_3 at RT, and annealed to 200, 250, and 300 °C, respectively. LEIS spectra show that Cr remains on the surface, whereas Mn goes to the subsurface after annealing to 200 °C.

intense Cr peak appeared at ≈ 875 eV. The intensity of the Cr peak dropped and becomes almost the same intensity as the Se peak after annealing to 200 °C. It is important to point out, though, that the peak intensity depends on many factors including the ion neutralization cross-section when scattering from atoms and thus the intensities in LEIS cannot be related to surface atom concentrations directly. The Cr, Se, and Bi peak intensities remain similar at 250 °C and 300 °C, which signifies that Cr stays on the surface even after annealing to 300 °C.

In contrast, when we repeat the experiment with Mn instead of Cr, the evolution of the LEIS spectrum at different temperatures is quite striking, as shown in Figure 2c. After room temperature deposition of Mn on Bi_2Se_3, an intense Mn peak appears at ≈ 900 eV, but with just annealing to 200 °C, the peak intensity drops and completely vanishes when annealed to 300 °C. At this temperature, the LEIS spectrum looks the same as pristine Bi_2Se_3. The evolution of the LEIS spectra denotes that, although Mn stays on the surface after room temperature deposition, after annealing to just 200 °C, it goes subsurface.

2.2. X-Ray Photoemission Spectroscopy

To understand more about the chemical state of the elements and their presence in the near surface region, we have performed XPS at each annealing step for the above-described experiments. **Figure** 3a shows Se-3d core level spectra for bare Bi_2Se_3, after Cr deposition on Bi_2Se_3 at RT, and after annealing to 200 °C. After Cr-deposition, the Se-3d peak has broadened and shifted to higher binding energy, which signifies that it has both Cr—Se and Bi—Se bonds. The intensity-count of the Se-3d peak increases once annealed to 200 °C, suggesting the diffusion of selenium from the bulk to the surface to react with Cr and form Cr_xSe_y (see Figure S1, Supporting Information, for XPS reference spectra of MBE grown Cr_xSe_y and metallic Cr). The Cr-2p core level spectra are shown in Figure 3b. The Cr peak is symmetric showing Cr—Se bonding. The intensity of the Cr-2p peaks remains the same after annealing, so there is no significant diffusion of Cr into the bulk at this temperature. The Cr-2p binding energy of 575.4 eV and 584.8 for Cr $2p_{3/2}$ and $2p_{1/2}$, is also close to that reported[21] previously for Cr_xSe_y compounds and the reference spectrum shown in Figure S1 (Supporting Information).

Figure 3c shows the Bi-4f core level spectra of pristine Bi_2Se_3 and after Cr deposition at RT and annealing to 200 ° C. For pristine Bi_2Se_3, Bi-4f XPS spectrum shows a single doublet. After deposition of Cr on Bi_2Se_3 at RT, we observe broadening of the Bi-4f peaks, which now can be fit with two components. The additional component is at a lower binding energy and can be attributed to metallic bismuth.[22,23] After annealing to 200 °C, the metallic component of bismuth decreases. A bismuth bilayer (Bi-BL) on top of Bi_2Se_3 is a stable structure,[24] and the bonding between one Bi_2Se_3-QL and one Bi-BL is stronger than between two Bi_2Se_3-QLs.[24,25] The formation energies of Bi-BL on the top of Bi_2Se_3 surface and inside the QLs are similar.[26] Thus, it is reasonable that after Cr-deposition, Cr extracts Se from the surface Bi_2Se_3-QLs to form Bi-BL and a Cr_xSe_y compound (see ABMID, below). With increasing annealing temperature Se can diffuse from the bulk to reform Bi_2Se_3 at the surface. From XPS and LEIS it appears that the Cr_xSe_y layer already formed after RT deposition of Cr, is stable at the surface which prevents Cr-diffusion into the Bi_2Se_3. This is also consistent with reports of MBE grown Cr_xSe_y layers[21] on Bi_2Se_3.

Similarly, we have performed chemical state analysis for the reaction of Mn with Bi_2Se_3 for stepwise annealed samples. The Se-3d core level spectra broadens only very slightly toward the higher binding energy side indicating a less pronounced change in the charge state of Se due to Mn—Se bonds compared to Cr—Se as shown in Figure 3d (also see simulation of charge Mulliken population, below). Mn-2p core level spectra are shown in Figure 3e after monolayer amount of Mn deposited on Bi_2Se_3 at RT and annealed to 200 °C. Along with $2p_{3/2}$ and $2p_{1/2}$, two satellite peaks, which are the characteristics of the Mn^{2+} chemical state are observed,[27] see also Figure S1 (Supporting Information) for comparison to Mn co-deposited with Se. This indicates that monolayer amounts of Mn strongly bind to Se at the surface to form a 2+ state. After annealing Mn remains in a 2+ state but

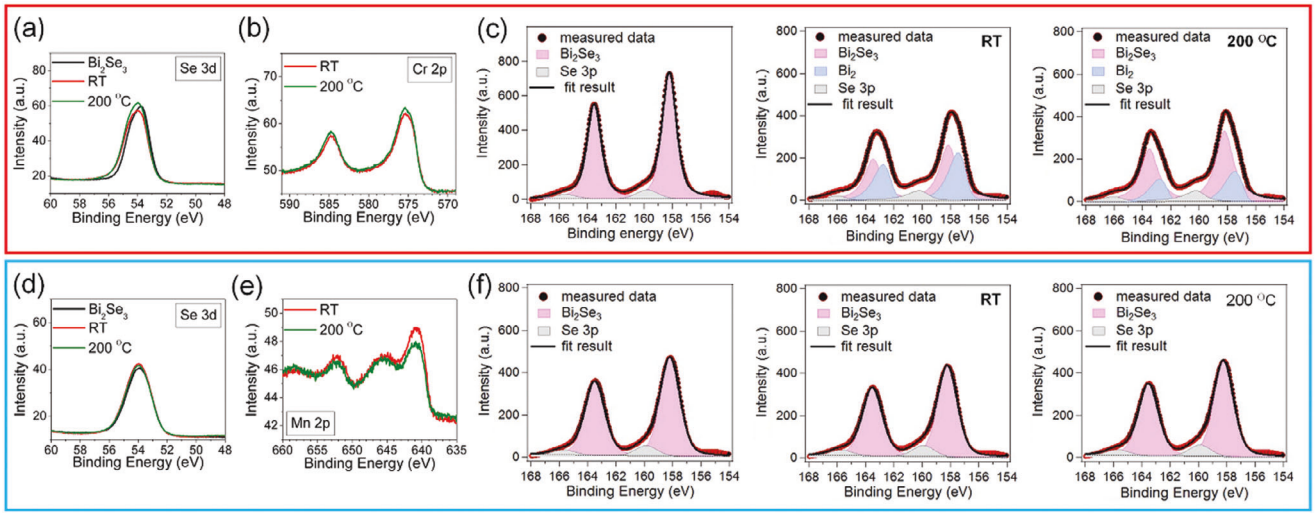

Figure 3. XPS analysis of reaction of Cr or Mn with Bi_2Se_3 single crystal a) Se-3d core level spectra of Bi_2Se_3, monolayer amount of Cr deposited on Bi_2Se_3 at RT, and after annealing to 200 °C b) Cr-2p core level spectra after deposition at RT and annealed to 200 °C. c) Bi-4f core level spectra for (i) Bi_2Se_3, (ii) after monolayer amount of Cr deposition at RT, (iii) annealed to 200 °C. The two Bi-4f components are fitted with pink (Bi-Se) and blue (Bi-Bi) colors. The grey color peak corresponds to Se-3p. d) Se-3d peak of Bi_2Se_3, monolayer amount of Mn deposited on Bi_2Se_3 at RT, and after annealed to 200 °C. e) Mn-2p core level spectra after deposition at RT and annealed to 200 °C. f) Bi-4f XPS spectra of (i) Bi_2Se_3, (ii) after monolayer amount of Mn deposition at RT, (iii) and annealed to 200 °C.

decreases slightly in intensity, consistent with the LEIS data that shows that Mn diffuses below the surface. The relatively small attenuation suggests, however, that Mn remains close to the surface as expected for the formation of a $MnBi_2Se_4$ compound (see Figure 1b). In contrast to Cr, small amounts of Mn do not induce a strong change in Bi 4f core levels, shown in Figure 3f. This indicates that Bi remains in Bi_2Se_3 environment and Mn only binds to the surface Se without extracting it from the Bi_2Se_3. Upon annealing Se again diffuses to the surface and Mn diffuses sub-surface to form the $MnBi_2Se_4$ compound.

2.3. Scanning Tunneling Microscopy

An STM topography and line profile of pristine Bi_2Se_3 is shown in Figure S2a (Supporting Information), with an atomically resolved image at the inset. The step height of ≈1 nm in the line profile corresponds to the 1 QL of Bi_2Se_3. STM images are acquired after each deposition or annealing step to detect the morphological changes of the surface. Following the deposition of a close-to-monolayer amount of Cr at RT, we observe islands with a height of 0.6 nm. This height agrees with reports[21] of Cr_xSe_y van der Waals layers. In between these van der Waals islands, Cr induced surface disorder is observed, as shown in **Figure** 4a. We have taken atomically resolved image of one of the islands that shows a hexagonal pattern as expected for a transition metal dichalcogenides (TMDs), but Cr insertion in between the TMD layer and the Bi_2Se_3 substrate is possible. After annealing the sample to 200 °C, the tiny islands expand, and the surface also becomes atomically smooth again, as shown in Figure 4b, suggesting that disordered Cr on the surface diffuses and reacts with Se to form Cr_xSe_y islands. Drawing a line profile in a region where a few layers of Bi_2Se_3 are shown, the thickness of the immediate layer beneath the randomly shaped Cr_xSe_y islands is around 0.4 nm, indicating the formation of Bi-BL at the interface, as shown in Figure 4b and Figure S2b (Supporting Information). From LEIS, XPS, and STM analysis, we thus conclude that by surface reaction of monolayer amount of Cr with Bi_2Se_3, a $Cr_xSe_y/Bi_2/Bi_2Se_3$ heterostructure is obtained.

Akin Cr, we have taken STM images after close-to-monolayer of Mn deposition on Bi_2Se_3 at RT. At first glance, the topography looks similar to the Cr-deposited one, but there is some distinction. First, the island size is smaller, as shown in Figure 4c. The line profile shows that the height of the islands is mostly 0.6 nm, but a few thicker (1 nm) and thinner (0.3 nm) islands are also present. The height of the islands corresponds to multiples of the unit-cell height of the thermodynamically favored rocksalt structure of MnSe of ≈0.3 nm. Thus we tentatively assign these islands as rocksalt MnSe with the first Mn-layer bound to the surface Se of Bi_2Se_3 (0.3 nm tall) and a few MnSe bilayer islands.[28] The surface between the islands has not been roughened. We have acquired atomically resolved image of this area and it shows the same hexagonal pattern as pristine Bi_2Se_3.

After annealing the system at 200 °C, the ad-islands disappeared, and elongated islands form, as shown in Figure 4d. The step height of these islands is around 0.4 nm from the background. This step height is the difference between Bi_2Se_3 and $MnBi_2Se_4$, i.e., MnSe embedded in Bi_2Se_3 (Figure 1b).[28,29] The elongated shape of these islands may suggest an elastic strain relaxation mechanism.[30] Such strain may be expected for a $MnBi_2Se_4$ layer embedded in Bi_2Se_3, due to the slightly different lattice constants between these compounds (a_{Bi2Se3} = 4.14 Å and $a_{MnBi2Se4}$ = 3.9 Å).[29,31] In zoomed in images we can also observe buckling on the islands as shown in the inset of Figure 4d. This kind of modulation is further evidence of stress in the lattice.[32]

Importantly, STM demonstrates that for both reactions of Bi_2Se_3 with Cr or Mn the surface remains well ordered and 2D

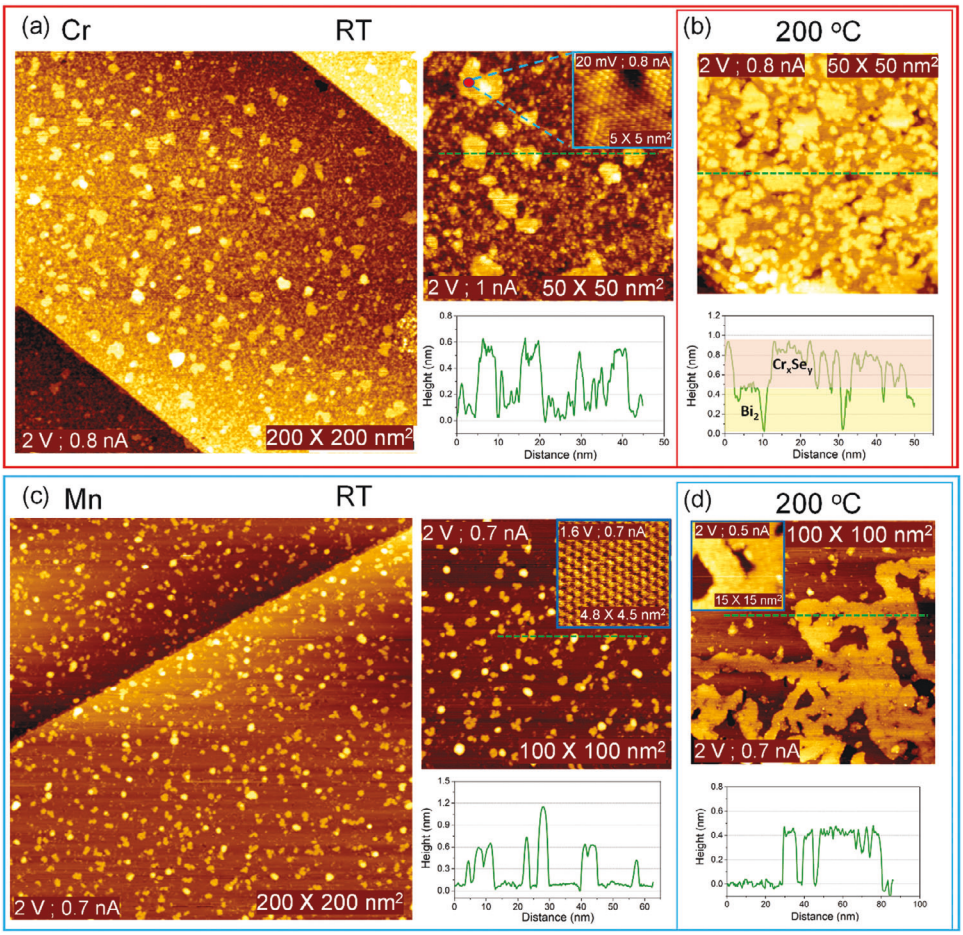

Figure 4. Scanning tunneling microscopy (STM) of Cr or Mn deposition on Bi_2Se_3 at RT and subsequent annealing to 200 °C. a) STM image of Cr deposited on Bi_2Se_3 at RT. The line profile of the tiny Cr_xSe_y islands is shown. A zoomed-in area where the islands are visible with Cr induced surface disorder in the background. An atomically resolved image is taken on an island showing the hexagonal pattern. b) The STM image after the sample is annealed to 200 °C. The Cr clusters are reacted with selenium to form uniform coverage of Cr_xSe_y. The line profile shows that the height of the immediate layer beneath randomly shaped Cr_xSe_y is around 0.4 nm, which suggests the presence of Bi-BL. We have used light yellow and pink colors as a guide to the eye in STM images to show Bi-BL and Cr_xSe_y layers, respectively. c) Topography of Mn deposited on Bi_2Se_3 at RT. The small islands of MnSe nucleate uniformly on the surface of Bi_2Se_3. The line profile shows that most of the islands have a thickness of around 0.6 nm. The atomically resolved image of the background in the inset shows the hexagonal pattern of Bi_2Se_3. d) The morphology changed after annealing to 200 °C. Elongated-shaped islands form with a height of 0.4 nm. The inset shows a zoomed-in image exhibiting buckling on the surface.

terraces are formed. This justifies the interpretation of LEIS and XPS as uniform layered systems.

2.4. Combined Analysis of LEIS, XPS, and Native Point Defects

Cr/Se intensity ratio in LEIS and the Cr-2p XPS peak intensity are plotted as a function of temperature in **Figure 5**a. The Cr/Se LEIS ratio is close to 2.5 at RT and becomes almost one after annealing. The XPS intensity of Cr-2p retains almost 80% of its initial value during annealing. The two Bi-components assigned to Bi_2Se_3 and metallic Bi, respectively, are plotted in Figure 5b. The metallic bismuth component is most intense at RT and then drops gradually with annealing. We interpret these results as depicted by the schematic on top at different temperature domains. After Cr deposition at RT, Cr_xSe_y forms, but complete selenization of Cr occurs after annealing to 200 °C. The evolution of the Bi-Bi component suggests that Bi_2 layer is already formed at RT indicating high mobility of Se and its reaction with Cr. After annealing, some of the Bi_2 either selenizes to reform to Bi_2Se_3 or diffuses into the bulk.

Similarly, Figure 5c shows the evolution of Mn/Se LEIS intensity and Mn-2p XPS peak intensity with annealing to different temperatures. There is a sudden drop from 2.5 to 0.3 in LEIS intensity after annealing to 200 °C, then completely zero at 300 °C. The maximum drop in Mn-2p intensity is from 250 to 300 °C. The Bi-Se and Bi-Bi components of the Bi-4f core level spectrum are plotted in Figure 5d to highlight the absence of metallic Bi and its minimal change in contrast to its behavior for Cr. The graphical schematics on top illustrate the structural changes based on the combined experimental observations. MnSe forms on the surface of the Bi_2Se_3 in the first temperature window. Then, Mn diffuses sub-surface to form $MnBi_2Se_4$ in the second temperature regime. Here, the surface sensitivity of LEIS and XPS plays a significant

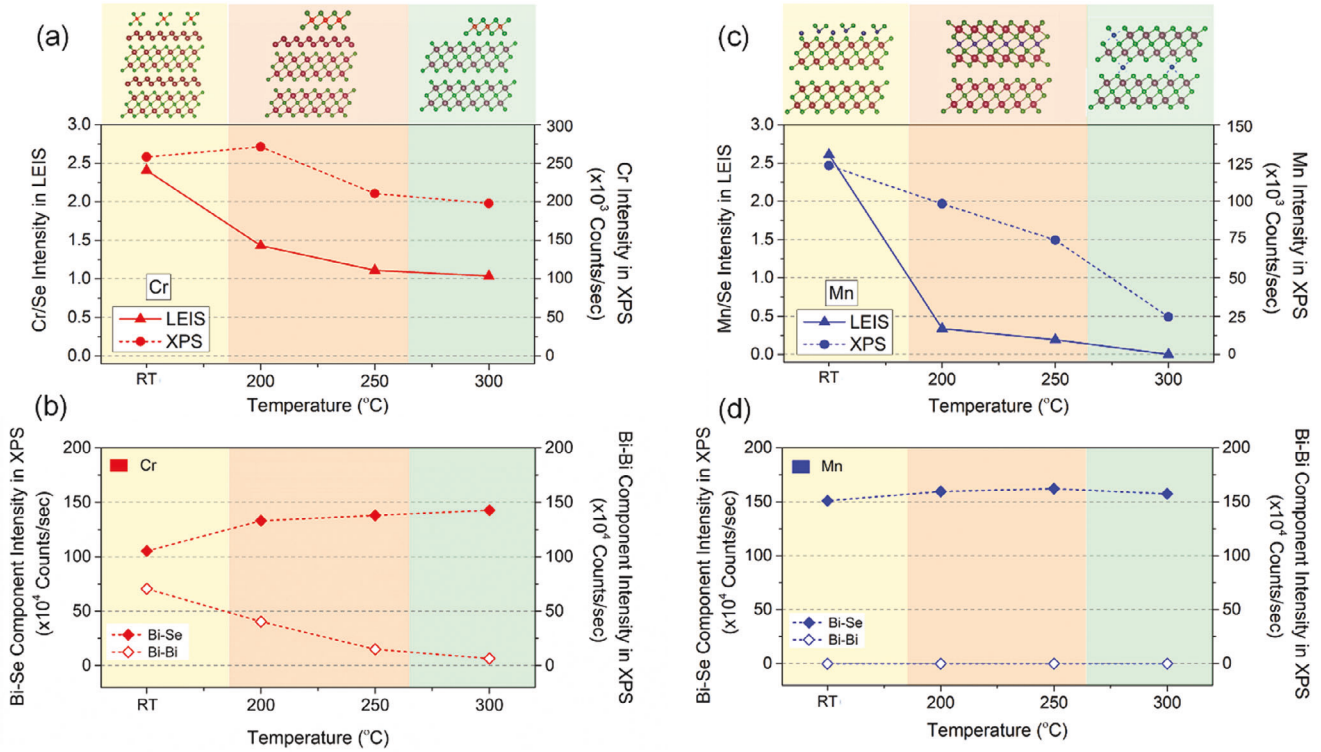

Figure 5. XPS and LEIS analyses of solid state reaction epitaxy of Mn or Cr with Bi_2Se_3. a) Cr/Se intensity in LEIS and Cr-2p intensity counts in XPS are plotted as a function of temperature. b) The evolution of the two components (Bi-Se and Bi-Bi) of the Bi-4f XPS peak with temperature is shown. The schematic on top depicted probable structural modification. The Cr/Se LEIS intensity ratio is highest at RT and almost becomes close to 1 after annealing. The metallic bismuth component is most prominent at RT and gradually drops with subsequent annealing, and the Bi-Se component increases. c) The Mn/Se intensity ratio in LEIS and Mn-2p intensity counts in XPS are plotted at different temperatures. Initially, the ratio is close to 2.5, but there is a sudden drop following the annealing. d) The Bi-Se and Bi-Bi components are plotted here as well for comparison. The graphic illustration on top shows three types of structural reconstruction. At RT, MnSe is on the surface, embedded in Bi_2Se_3 in the second temperature window, and goes to bulk at 300 °C.

role. In XPS, the intensity retains 80%–60% of its initial count, but LEIS intensity drops to less than 10% of its initial value. At 300 °C, the Mn-LEIS intensity drops to zero and the Mn-2p XPS intensity also decreases substantially, denoting diffusion of Mn into the bulk or inside the vdW gap. The absence of a metallic bismuth component throughout Mn deposition and annealing denotes that the required Se for the reaction epitaxy comes from the bulk crystal.

Interestingly, the intensity counts for LEIS in the middle-temperature range is not zero, where all the experimental analyses suggest the formation of the $MnBi_2Se_4$. Mn is in the fourth atomic layer of this phase and should not be detected by LEIS. The origin of this weak Mn-signal in LEIS can be understood by atomically resolved STM studies of this temperature window. The STM topography and the atomically resolved image are shown in **Figure** 6a after annealing the sample at 250 °C. We can locate two types of point defects, either dark triangles (type A) or bright dots (type B).[33] After annealing the sample to 300 °C, the large-scale topography becomes completely flat, the dark triangle defects disappear, and only bright defects remain, as shown in Figure 6b. The dark triangle-defects (type A) have been identified previously as Mn at Bi antisite defects (Mn_{Bi})[15,29,34] in the second atomic layer of $MnBi_2Se_4$. This is a characteristic defect of the $MnBi_2Se_4$ phase and thus further supports the formation of this phase. The bright dot defects are possibly due to the Bi or Mn substitution of Se on the topmost layer (Bi_{Se} or Mn_{Se}). The uniformity of this type B defect is retained at 300 °C as well when the Mn peak vanishes from the LEIS spectrum and thus are more likely Bi_{Se} defects. Consequently, the combined LEIS and atomic resolved STM analysis shows that monolayer amounts of Mn reacts with Bi_2Se_3 to form $MnBi_2Se_4$ but with significant amounts of Mn_{Bi} antisite defects in this phase. Higher annealing temperature causes the dissolution of the Mn into the bulk of Bi_2Se_3.

2.5. Ab Initio Molecular Dynamics simulations

Quantum molecular dynamics simulations offer an opportunity to explore the temporal evolution of complex systems at the atomic scale. In this work, ab initio molecular dynamics (AIMD) calculations were carried out to investigate the dynamics for Cr and Mn atoms interacting with Bi_2Se_3 layers. The main objective of the simulations is to provide insights on differences in the initial reactions of the two TM (Mn and Cr) with Bi_2Se_3 in an attempt to obtain atomistic information on the differences of the two TM considered. For all cases, we can observe the diffusion of the Se atoms toward the TM, structurally evolving to the initial formation of a TM-Se structure, while the Bi-Bi distances decrease. It

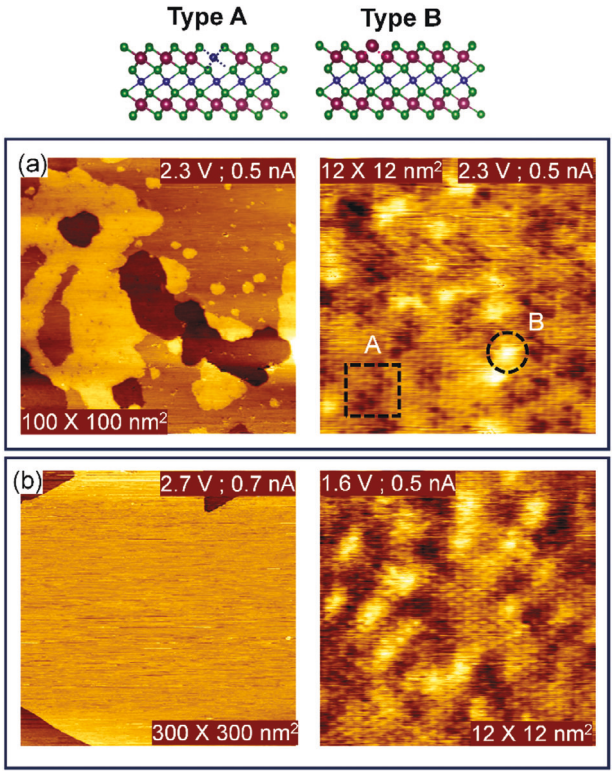

Figure 6. Scanning tunneling microscopy (STM) of Mn deposition on Bi_2Se_3 and subsequent annealing to 250 °C and 300 °C. a) After annealing to 250 °C, two types of defects are visible, dark triangles (type A) and bright dots (type B). The type A defect corresponds to Mn in the Bi site (Mn_{Bi}) in the second atomic layer, and the type B defect denotes Bi substitution of Se on top (Bi_{Se}), as shown in the schematic. b) The topography becomes flat following the annealing at 300 °C. The dark triangular defects disappear, and bright defects remain.

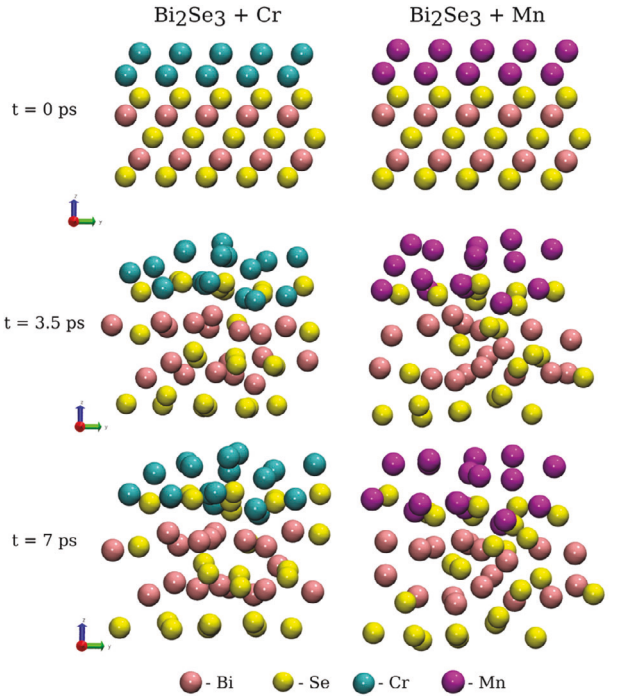

Figure 7. Representative AIMD snapshots of the systems (Bi_2Se_3 + Cr (left) and Bi_2Se_3 + Mn (right)) at different stages of the simulations. Initial configuration (t = 0 ps, top), intermediate (t = 3.5 ps, middle), and final (t = 7 ps, bottom).

must be taken into account that the simulations are computationally expensive, but our results show that 7 ps is sufficient for the system to stabilize, as shown in Figure S5 (Supporting Information).

For the AIMD simulations, a Bi_2Se_3 monolayer with a bilayer of Cr/Mn on top of Bi_2Se_3 was constructed representing the initial configuration before the diffusion. It is worthwhile pointing out that this is a simplified model and does not entirely capture the more complex experimental situation where single atoms are deposited. However, in the experiment metals are initially deposited at RT and the reaction occurs at slightly elevated temperature, so that an initial formation of a metal layer may not be entirely unrealistic. The main objective of the simulations is to obtain insights on the diffusion of Se in the presence of metal atoms. The transition metal atoms were positioned on top of the Bi atoms of the first and second atomic layers. The AIMD snapshots for t = 0 ps, t = 3.5 ps, and t = 7 ps are shown in **Figure 7**, and the time evolution of the AIMD simulations can be found in Videos S1 and S2 (Supporting Information). Initially, we can observe the migration of the top Se atoms toward the adsorbed Cr-atoms while the outer bottom Se layer does not present any apparent diffusion, as seen by the snapshots at t = 7 ps. At subsequent simulation times, the thermalization of the system causes the increase of the disorder, dissipating structural strain (Figure 7). The diffusion of the Se atoms toward adsorbed TMs, clearly shows the initial stages of the reaction of the TMs with the Se of the Bi_2Se_3 and is in agreement with the experimental observations that adsorbed TM convert into selenides by extracting the selenium from the Bi_2Se_3. The simulation results also show that Bi atoms do not interact with the TM and move closer to each other, which may ultimately lead to the formation of the experimentally observed Bi bilayer.

Visually (from the Figures and movies), it is not possible to determine if the Se atoms have more affinity for Cr or Mn. To obtain a more quantitative analysis, we calculated the charge Mulliken population (MP) for the top Se and metal atoms at the beginning and end of the simulations. The results are presented in Figure S6 (Supporting Information). It is possible to see a decrease in the spin-up population of Se atoms at the beginning and at the end of the simulation while the spin-down population increases. Figure S7 (Supporting Information) shows the MP for the Bi atoms in the Cr/Mn bilayer system. We can see that after 7 ps of the simulation, there is a slight but noticeable change in the MP of Bi for the Cr systems, whereas no significant changes are observable for the Mn case.

Based on the MP analyses, we further investigate the possibility of a Bi formation when both top and bottom Se atoms are exposed to Cr atoms by considering a structural model in which two Cr monolayers sandwich a Bi_2Se_3 monolayer. The model was created by placing Cr atoms in 1:1 proportion with Bi, where half of these Cr atoms are added as a monolayer on top and the other half monolayer is placed at the bottom of a pre-optimized Bi_2Se_3

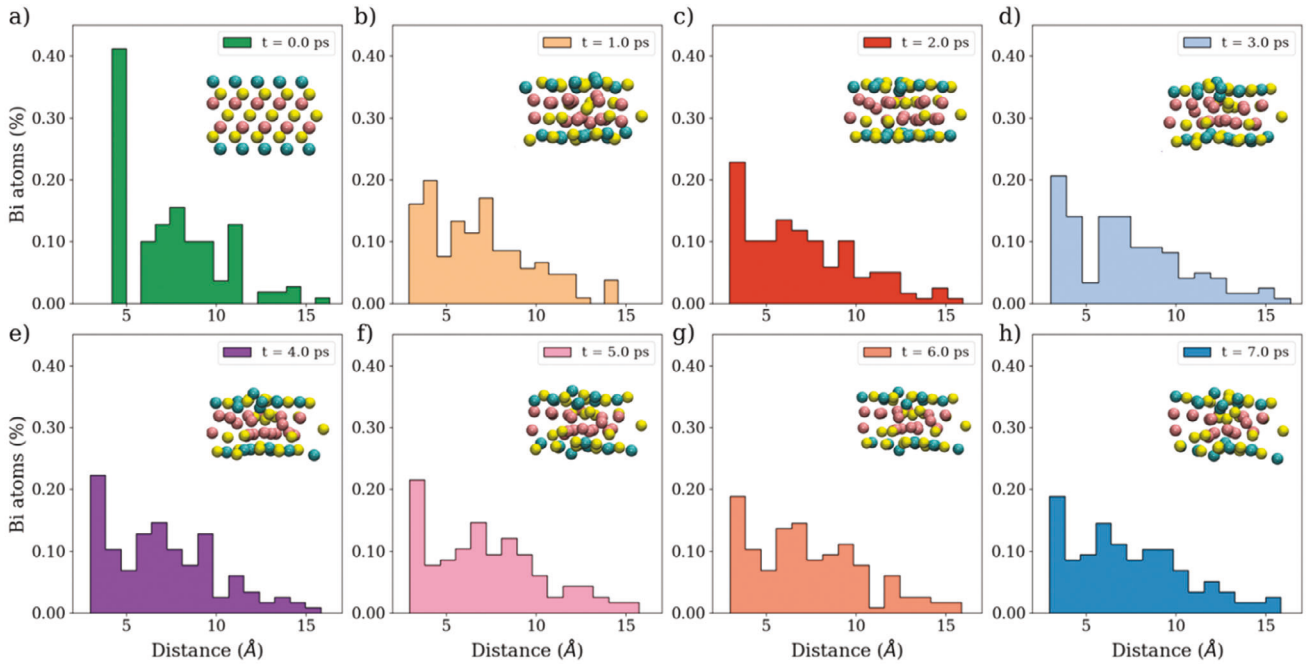

Figure 8. Distribution of the distances between Bi atoms at a) t = 0 ps, b) t = 1 ps, c) t = 2 ps, d) t = 3 ps, e) t = 4 ps, f) t = 5 ps, g) t = 6 ps, and h) t = 7 ps.

surface (inset of Figure 8a). While this model is unrealistic in relation to the experiments, it is used to obtain theoretical insights on the diffusion of Se and formation of Bi bilayer since, in this model, both Se outer layers are exposed to Cr. Here, the Se atoms tend to migrate toward Cr, and an initial diffusion of the middle Se atoms is noticeable. Within this model, middle Se atoms could migrate to the top or bottom layer, facilitating the formation of Bi bilayer within the accessible simulation time, in contrast to the model with a bilayer on top of Bi_2Se_3 (see also Figure S8, Supporting Information). We used the geometrical output data from the AIMD simulations to investigate the relative distances between the Bi atoms during the simulation. In **Figure 8**, we present the distribution of the distances between neighbor Bi atoms and the corresponding AIMD snapshots along different times of the simulations (t = 1–7 ps). At t = 0 ps, the distance between neighboring Bi atoms is around 4.5 Å, consistent with Bi_2Se_3 with a Se layer in between Bi atoms. At further time steps, the diffusion of top and bottom Se atoms toward Cr creates stronger interactions between the central Bi atoms, which come closer to each other. This is further evidenced by the decrease in the distances between neighboring Bi atoms, indicated by the shift of the larger peak below 4.0 Å, as seen in Figure 8(b-h). The final structure (presented in Figure 8h, shows a few remaining Se atoms at the middle layer, indicating that the Bi atoms are indeed moving toward the formation of the bilayer. This result is further supported by Figure 8h, in which we can see that in the final distance distribution, a large percentage of Bi atoms are within d < 4.0 Å, indicating the Bi atoms are now close to each other. For comparison, the distance between Bi atoms in Bi-bulk ranges between 3.2 and 3.4 Å. These values were obtained from the most stable Bi structures from the Materials Project database and shown in Figure S9 (Supporting Information), namely Bi with R3m symmetry (mp-23152) and Bi with Pm3m symmetry (mp-567597).

2.6. Varying Metal Amounts and Metal and Selenium Co-Deposiiton

So far, we have studied the close to ideal amount (one monolayer) of metal deposition on Bi_2Se_3 that is required to form a XBi_2Se_4 monolayer compound. We also conducted experiments with smaller amounts of Cr or Mn. Under these conditions both Cr and Mn atoms tend to diffuse into the bulk and form diluted dopants as is shown in Figure S3 (Supporting Information).

Increasing the amount of deposited Mn to multilayers, also changes the behavior significantly. In this case, a stable MnSe adlayer is formed by reacting with substrate Se as shown in Figure S4 (Supporting Information). Similar to Cr deposition, Se is extracted from the Bi_2Se_3 surface layer forming metallic Bi, as observed in XPS (Figure S4a, Supporting Information) and supported by AIMD simulations. Initially, the intensity of the Se-3d XPS spectrum dropped after 3–4 layers of Mn deposition at RT. Subsequent to annealing at 200 °C and 250 °C, The Se-XPS intensity increased significantly and moved toward higher binding energy, as shown in Figure S4b (Supporting Information). The Mn-2p XPS spectra also changes from predominantly metallic at RT to a 2+ state with characteristic satellite peaks after annealing to 250 ° C. Interestingly, the Mn peak intensity in the LEIS spectrum remains the same or even increases with annealing up to 250 °C (Figure S4d, Supporting Information); this shows that Mn stays on the surface instead of diffusing to the sub-surface. Thus, multilayer Mn is transformed into MnSe film that remains

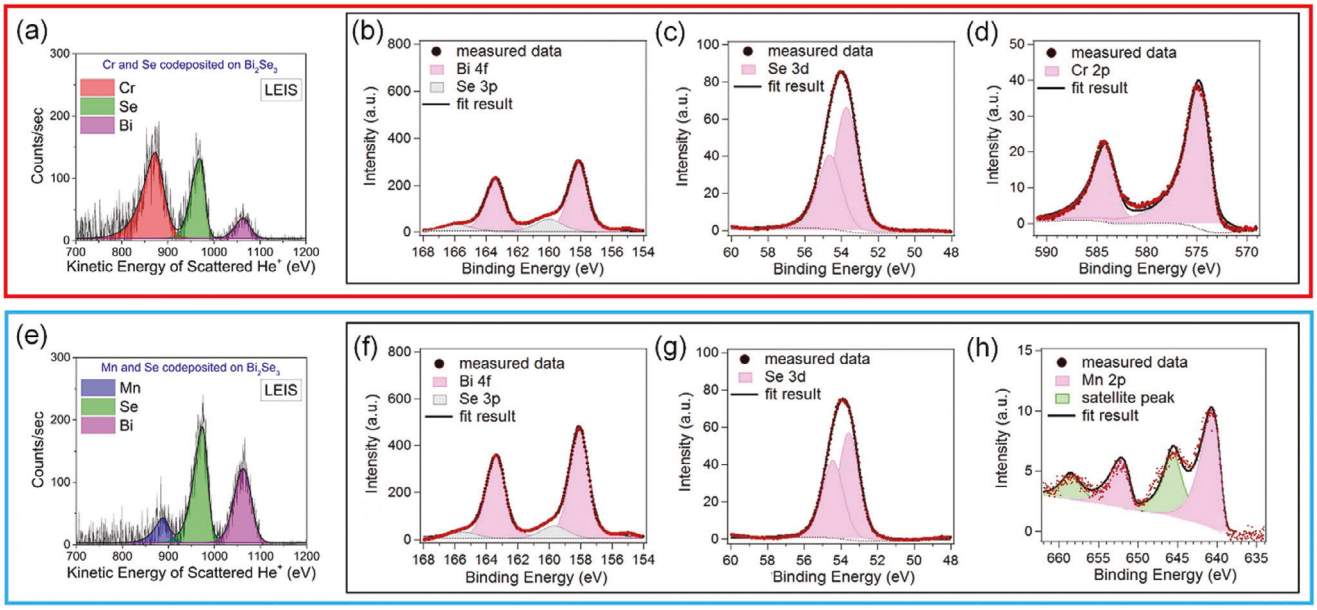

Figure 9. LEIS and XPS characterization of Cr, Se, and Mn, Se co-deposited on Bi_2Se_3. a) LEIS spectrum shows peaks corresponding to Cr and Se with almost the same intensity with a small Bi peak. b) Bi-4f, c) Se-3d, and d) Cr-2p core level spectra for Cr_xSe_y and Bi_2Se_3 heterostructure. The intensity count for the Bi-4f peak dropped significantly. e) LEIS spectrum shows peaks corresponding to Mn, Se, and Bi. The Mn peak intensity is minimal compared to Se and Bi. f) Bi-4f, g) Se-3d, h) and Mn-2p core level spectrum of $MnBi_2Se_4$. The satellite feature for Mn suggests that it is in a 2+ state.

at the surface and no evidence for the formation of $MnBi_2Se_4$ is observed for such multilayers. This suggests that the stability of the adlayer plays an important role in the solid state reaction between Mn and Bi_2Se_3. For Cr, no significant difference between monolayer and multilayer deposition is observed in both cases, the Cr_xSe_y adlayer is the preferred structure.

The suppression of interface reaction for both Mn and Cr is preceded by extraction of Se from Bi_2Se_3 and the formation of metallic Bi. To investigate the potential role of the formation of a selenium deficient layer in suppression of interface reactions, we co-deposited Mn and Cr in a Se background to avoid Se depletion in Bi_2Se_3 substrate.

We co-deposited monolayer amounts of metal (Cr or Mn) together with selenium. The deposition rate of Se was about 10 times higher than that of the metal to achieve full selenization of the metals. To avoid sticking of excess Se on the surface during deposition, the deposition temperature was chosen above the evaporation temperature of elemental Se from the surface at 300 °C.

For Cr co-deposited with Se, **Figure 9a** shows the LEIS spectrum with quite an intense Cr peak. The intensity ratio of Cr and Se is almost the same, and there is only a small Bi peak. This LEIS spectrum indicates that Cr remains at the surface. Figure 9b shows that the intensity count of the Bi-4f XPS peak dropped significantly. As anticipated there is no metallic component for Bi-4f, as Cr was co-deposited with Se. The Se 3d peak broadened and shifted toward higher binding energy indicating that Se has components from Bi_2Se_3 and Cr_xSe_y, Figure 9c., Cr-2p peak shape is again consistent with Cr-Se bonding in Figure 9d. The attenuation of Bi-4f peak intensity and the strong Cr-peak in LEIS indicates that we again obtain a Cr_xSe_y/Bi_2Se_3 heterostructure instead of a $CrBi_2Se_4$ septuple layer.

When Mn and Se are co-deposited on Bi_2Se_3 at 300 °C we can detect only a very small Mn peak plus notable Se and Bi peaks in the LEIS spectrum as shown in Figure 9e. This indicates that Mn is not on the surface. Figure 9f,g shows Bi-4f and Se-3d XPS peaks. There is no strong attenuation of the Bi-4f peak, which again indicates the absence of MnSe on the surface. The XPS intensity count of Mn-2p, however, is high, revealing that Mn is not deep in the bulk. Mn-2p core level spectrum in Figure 9h shows a satellite peak denoting the Mn^{2+} state, consistent with $MnBi_2Se_4$. Thus, we conclude that the reaction of just the TM with Bi_2Se_3 results in similar structures as the co-deposition of TM in a selenium background. The Bi_2Se_3 bulk sample provides a sufficient source of Se to form TM-selenide adlayers, which has also been exploited previously to form various selenide thin films on Bi_2Se_3.[31,35] The $CrBi_2Se_4$ phase is also not obtained by co-deposition of Cr and Se. This observation let us conclude that the Bi-bilayer, which forms at the interface between Cr-selenide and Bi_2Se_3 by reacting Cr with Bi_2Se_3 is not the reason for preventing the formation of a $CrBi_2Se_4$ phase.

3. Conclusion

We have studied the reaction of two TMs, Cr and Mn, with Bi_2Se_3. Both TM interact strongly with Se and can form TM-selenide adlayers. The stability of these adlayers and the availability of stable secondary phases determines the interface reactions. $Cr_{1+\delta}Se_2$ is a stable pseudo 2D material (i.e., a vdW material with self-intercalated Cr in between layers). Such 2D materials are stable even as monolayers. Thus, once formed by reacting with Se (either from the Bi_2Se_3 substrate or supplied by co-deposition during MBE growth) it does not convert into the desired $CrBi_2Se_4$. This is contrasted with MnSe, which is not a stable 2D material,

and thus a monolayer grown on Bi_2Se_3 can convert into a more stable phases by reacting with Bi_2Se_3 to $MnBi_2Se_4$. Multilayers of MnSe are more stable and this suppresses its solid state reaction with Bi_2Se_3. We also showed both experimentally as well as by AIMD simulations that the reaction of TM with Bi_2Se_3 can proceed at low temperatures by extracting Se from just the surface layer to form metallic Bi-bilayers. This is the case if this reaction occurs at low enough temperatures at which Se-diffusion from the bulk is not activated sufficiently to compensate for the Se-loss in the surface layer. This allows for the synthesis of a Bi-bilayer in between the Bi_2Se_3 bulk and a TM-selenide overlayer. We have seen that this is possible for Cr but not for Mn-monolayers, indicating again a delicate balance between the chemical potential of the different phases and the observed transformations. Overall, this study shows the potential for synthesizing complex vdW heterostructures by solid state reactions. The $MnBi_2Se_4$ phase on the surface of Bi_2Se_3 is sought for combining magnetic vdW materials with topological materials. On the other hand, the bismuth bilayer between Bi_2Se_3 and Cr_xSe_y is another component with high spin orbit coupling that could enhance the probability for the formation of skyrmions.[36] Opportunities to engineer 2D materials by solid state reactions should not be limited to Bi_2Se_3, but other 2D materials may be transformed by reacting with TM. This for instance has been shown for the formation of intercalated atoms in transition metal dichalcogenide[37] and may be an approach for synthesizing multi-TM 2D materials (e.g., the ferromagnetic 2D materials Fe_3GeTe_3 or $Cr_2Ge_2Te_6$) from single-TM 2D (e.g., $Cr_{1+\delta}Te_2$) monolayer or bulk materials.

4. Experimental Section

Synthesis: Bi_2Se_3 single crystal substrate was freshly cleaved in air and inserted inside the UHV chamber. The surface of Bi_2Se_3 was cleaned by a few repeated cycles of Ar^+ ion sputtering and vacuum annealing at 400 °C for around 30 min. Chromium was evaporated from a 2 mm ultrapure metal rod attached to a mini e-beam evaporator. Manganese was also deposited from a mini e-beam evaporator but the Mn was contained in a Ta-crucible. The metals were deposited on Bi_2Se_3 held at RT and subsequently annealed to different temperatures. For the co-deposition of metals and selenium (Se), Se was provided from a thermal cracker source. All sources were cooled with continuous water flow. For comparison of solid-state reaction epitaxy, Cr_xSe_y, and Mn_xSe_y were also grown on HOPG by co-deposition of metal and Se, with HOPG substrate temperature of 300 °C. Succeeding to each deposition or annealing steps, samples are characterized by XPS, LEIS, and STM techniques.

XPS: After each deposition or annealing step, the samples are transferred from the preparation chamber to a surface science analysis chamber for XPS and LEIS studies without breaking vacuum. For XPS, a non-monochromatized dual anode X-ray (Mg-Kα) source was employed for photoexcitation, and an Omicron Sphera hemispherical analyzer for photoelectron detection. The binding energy of C-1s (284.8 eV) of the HOPG substrate was used for calibration.

LEIS: Low energy ion scattering spectroscopy was executed with a differentially pumped focused extractor noble gas ion source (SPECS IQE 12/38). He^+ ions with an energy of 1200 eV were used and scattered with a fixed scattering angle of 130°. The same electrostatic hemispherical analyzer (Omicron Sphera Analyzer) as for XPS was used in reversed polarity for the detection of the scattered He^+ ions. To check the sensitivity of the LEIS setup, we grew a small amount of MnSe on the HOPG substrate. The Mn-2p XPS intensity is much lesser than the sub-monolayer amount of Mn deposited on Bi_2Se_3, as shown in Figure S10a (Supporting Information). The Mn peak intensity in the LEIS spectrum (Figure S10b, Supporting Information) for the same MnSe sample on HOPG is significant. It suggests that even a tiny amount of Mn can be detected by the LEIS setup when it is on the surface.

STM: Scanning tunneling microscopy measurements are performed with an Omicron VT-STM operated at room temperature. STM tips are made with electrochemically etched tungsten wires and cleaned by in situ voltage pulsing.

AIMD: The structural models used in the AIMD simulations were created as follows: first, the Bi_2Se_3 surface (composed of a Bi_2Se_3 monolayer) is fully optimized. Hereafter, we use the term Bi_2Se_3 surfaceslab to refer to a Bi_2Se_3 monolayer. Then, the Cr/Mn bilayer is modeled by considering a 1:1 proportion with the Bi atoms in one Bi_2Se_3 monolayer/slab. Then, this bilayer is added on top of the Bi_2Se_3 surface. While the surface (in the absence of Cr/Mn atoms) is at an energy minimum when the metal atoms are added the system is no longer stable and can react. As the AIMD simulations are very expensive and we are running only for 7 ps, in order to speed up the reactions, the Cr/Mn atoms are initially deposited in the interaction range with the slab. We stress that these simplified structural models are used mainly to investigate the behavior of the Bi_2Se_3 surface in the presence of Cr/Mn atoms in the AIMD context. AIMD was carried out using the SIESTA code.[38] We used the vdW-DF (DF1) functional[39] to treat the exchange and correlation interactions, taking into account van der Waals corrections. Valence electrons were expanded using a double-ζ polarized basis set, and a cutoff mesh of 200 Ry was used for the real space. The self-consistency convergence criterion was set to 10^{-7} eV, while energy and forces convergence thresholds were set to 10^{-4} eV and 0.01 eV/A, respectively. Brillouin zone was sampled within the Monkhorst–Pack scheme[40] with an 8×8×1 and 2×2×2 k-point mesh for self-consistent and AIMD calculations. Since we are interested in the dynamics of the Cr/Mn interacting with Bi_2Se_3 layers, the canonical ensemble (NVT) was used, coupled to a Nosé–Hover thermostat at T = 500 K. The system was integrated for 7000 timesteps of 1 fs each.

Supporting Information

Supporting Information is available from the Wiley Online Library or from the author.

Acknowledgements

Financial support from the National Science Foundation under award DMR 2118414 was acknowledged. Financial support from the Brazilian Agencies CNPq and FAPESP was also acknowledged. PASA and CCO thank PRH-ANP (PRH.49-UFABC), CNPq (#308428/2022-6) for financial support and CCM-UFABC for the computational resources provided. DSG acknowleges support from FAPESP/CEPID Grant #2013/08293-7.

Conflict of Interest

The authors declare no conflict of interest.

Data Availability Statement

The data that support the findings of this study are available from the corresponding author upon reasonable request.

Keywords

ab initio molecular dynamics, Bi_2Se_3, low energy ion scattering spectroscopy, quantum materials, scanning tunneling microscopy, solid state reactions, surface modifications, X-ray photoemission spectroscopy

Received: November 28, 2023
Revised: March 1, 2024
Published online:

[1] S. J. Cho, M. J. Uddin, P. Alaboina, in *Emerging Nanotechnologies in Rechargeable Energy Storage Systems*, (Eds.: L. M. Rodriguez-Martinez, N. Omar), Elsevier, Boston, **2017**, p. 83.
[2] B. Wang, Y. Z. Ye, L. Xu, Y. Quan, W. X. Wei, W. S. Zhu, H. M. Li, J. X. Xia, *Adv. Funct. Mater.* **2020**, *30*, 2005834.
[3] X. Huang, J. Y. Tang, B. Luo, R. Knibbe, T. G. Lin, H. Hu, M. Rana, Y. X. Hu, X. B. Zhu, Q. F. Gu, D. Wang, L. Z. Wang, *Adv. Energy Mater.* **2019**, *9*, 1901872.
[4] J. G. Bednorz, K. A. Müller, *Z. Physik B – Condens. Matter.* **1986**, *64*, 189.
[5] S. N. Patankar, F. H. Froes, *Solid State Sci.* **2004**, *6*, 887.
[6] A. Kumar, S. Dutta, S. Kim, T. Kwon, S. S. Patil, N. Kumari, S. Jeevanandham, I. S. Lee, *Chem. Rev.* **2022**, *122*, 12748.
[7] T. Hirahara, S. V. Eremeev, T. Shirasawa, Y. Okuyama, T. Kubo, R. Nakanishi, R. Akiyama, A. Takayama, T. Hajiri, S. Ideta, M. Matsunami, K. Sumida, K. Miyamoto, Y. Takagi, K. Tanaka, T. Okuda, T. Yokoyama, S. Kimura, S. Hasegawa, E. V. Chulkov, *Nano Lett.* **2017**, *17*, 3493.
[8] T. C. Zhu, A. J. Bishop, T. Zhou, M. L. Zhu, D. J. O'Hara, A. A. Baker, S. Y. Cheng, R. C. Walko, J. J. Repicky, T. Liu, J. A. Gupta, C. M. Jozwiak, E. Rotenberg, J. Hwang, I. Zutic, R. K. Kawakami, *Nano Lett.* **2021**, *21*, 5083.
[9] E. K. Petrov, I. V. Silkin, T. V. Menshchikova, E. V. Chulkov, *JETP Lett.* **2019**, *109*, 121.
[10] E. K. Petrov, A. Ernst, T. V. Menshchikova, E. V. Chulkov, *J. Phys. Chem. Lett.* **2021**, *12*, 9076.
[11] Y. Xia, D. Qian, D. Hsieh, L. Wray, A. Pal, H. Lin, A. Bansil, D. Grauer, Y. S. Hor, R. J. Cava, M. Z. Hasan, *Nat. Phys.* **2009**, *5*, 398.
[12] M. Z. Hasan, C. L. Kane, *Rev. Mod. Phys.* **2010**, *82*, 3045.
[13] P. P. J. Haazen, J. B. Laloe, T. J. Nummy, H. J. M. Swagten, P. Jarillo-Herrero, D. Heiman, J. S. Moodera, *Appl. Phys. Lett.* **2012**, *100*, 082404.
[14] H. J. von Bardeleben, J. L. Cantin, D. M. Zhang, A. Richardella, D. W. Rench, N. Samarth, J. A. Borchers, *Phys. Rev. B* **2013**, *88*, 075149.
[15] C. Z. Chang, P. Z. Tang, Y. L. Wang, X. Feng, K. Li, Z. C. Zhang, Y. Y. Wang, L. L. Wang, X. Chen, C. X. Liu, W. H. Duan, K. He, X. C. Ma, Q. K. Xue, *Phys. Rev. Lett.* **2014**, *112*, 056801.
[16] H. L. Meyerheim, A. Ernst, K. Mohseni, A. Polyakov, I. V. Maznichenko, P. A. Buczek, A. Coati, S. S. P. Parkin, *Phys. Status Solidi B* **2021**, *258*, 2000290.
[17] F. Katmis, V. Lauter, F. S. Nogueira, B. A. Assaf, M. E. Jamer, P. Wei, B. Satpati, J. W. Freeland, I. Eremin, D. Heiman, P. Jarillo-Herrero, J. S. Moodera, *Nature* **2016**, *533*, 513.
[18] J. Y. Liu, T. Hesjedal, *Adv. Mater.* **2023**, *35*, 2102427.
[19] J. A. Hagmann, X. Li, S. Chowdhury, S. N. Dong, S. Rouvimov, S. J. Pookpanratana, K. M. Yu, T. A. Orlova, T. B. Bolin, C. U. Segre, D. G. Seiler, C. A. Richter, X. Y. Liu, M. Dobrowolska, J. K. Furdyna, *New J. Phys.* **2017**, *19*, 085002.
[20] H. H. Brongersma, M. Draxler, M. de Ridder, P. Bauer, *Surf. Sci. Rep.* **2007**, *62*, 63.
[21] M. Z. Liu, Y. L. Huang, J. Gou, Q. J. Liang, R. Chua, Arramel, S. S. D., L. Zhang, L. L. Cai, X. J. Yu, D. Y. Zhong, W. J. Zhang, A. T. S. Wee, *J. Phys. Chem. Lett.* **2021**, *12*, 7752.
[22] L. A. Walsh, C. M. Smyth, A. T. Barton, Q. X. Wang, Z. F. Che, R. Y. Yue, J. Kim, M. J. Kim, R. M. Wallace, C. L. Hinkle, *J. Phys. Chem.* **2017**, *121*, 23551.
[23] M. R. Scholz, J. Sanchez-Barriga, D. Marchenko, A. Varykhalov, A. Volykhov, L. V. Yashina, O. Rader, *Phys. Rev. Lett.* **2012**, *108*, 256810.
[24] H. S. Zhu, W. M. Zhou, J. A. Yarmoff, *Thin Solid Films* **2018**, *660*, 343.
[25] M. S. Christian, S. R. Whittleton, A. Otero-de-la-Roza, E. R. Johnson, *Comput. Theor. Chem.* **2015**, *1053*, 238.
[26] K. Govaerts, K. Park, C. De Beule, B. Partoens, D. Lamoen, *Phys. Rev. B* **2014**, *90*, 155124.
[27] Y. Ma, Y. J. Ma, G. T. Kim, T. Diemant, R. J. Behm, D. Geiger, U. Kaiser, A. Varzi, S. Passerini, *Adv. Energy Mater.* **2019**, *9*, 1902077.
[28] A. V. Matetskiy, I. A. Kibirev, T. Hirahara, S. Hasegawa, A. V. Zotov, A. A. Saranin, *Appl. Phys. Lett.* **2015**, *107*, 091604.
[29] R. C. Walko, T. C. Zhu, A. J. Bishop, R. K. Kawakami, J. A. Gupta, *Phys. E* **2022**, *143*, 115391.
[30] J. Tersoff, R. M. Tromp, *Phys. Rev. Lett.* **1993**, *70*, 2782.
[31] A. Cavallin, V. Sevriuk, K. N. Fischer, S. Manna, S. Ouazi, M. Ellguth, C. Tusche, H. L. Meyerheim, D. Sander, J. Kirschner, *Surf. Sci.* **2016**, *646*, 72.
[32] K. F. Zhang, F. Yang, Y. R. Song, C. H. Liu, D. Qian, C. L. Gao, J. F. Jia, *Appl. Phys. Lett.* **2015**, *107*, 121601.
[33] Y. H. Yuan, X. T. Wang, H. Li, J. H. Li, Y. Ji, Z. Q. Hao, Y. Wu, K. He, Y. Y. Wang, Y. Xu, W. H. Duan, W. Li, Q. K. Xue, *Nano Lett.* **2020**, *20*, 3271.
[34] L. G. Zhang, D. P. Zhao, Y. Y. Zang, Y. H. Yuan, G. Y. Jiang, M. H. Liao, D. Zhang, K. He, X. C. Ma, Q. K. Xue, *APL Mater.* **2017**, *5*, 076106.
[35] A. Polyakov, K. Mohseni, R. Felici, C. Tusche, Y. J. Chen, V. Feyer, J. Geck, T. Ritschel, A. Ernst, J. Rubio-Zuazo, G. R. Castro, H. L. Meyerheim, S. S. P. Parkin, *Nat. Commun.* **2022**, *13*, 2472.
[36] J. S. Chen, L. J. Wang, M. Zhang, L. Zhou, R. N. Zhang, L. P. Jin, X. S. Wang, H. L. Qin, Y. Qiu, J. W. Mei, F. Ye, B. Xi, H. T. He, L. Bin, G. Wang, *Nano Lett.* **2019**, *19*, 6144.
[37] V. Pathirage, S. Khatun, S. Lisenkov, K. Lasek, J. Li, S. Kolekar, M. Valvidares, P. Gargiani, Y. Xin, I. Ponomareva, M. Batzill, *Nano Lett.* **2023**, *23*, 9579.
[38] J. M. Soler, E. Artacho, J. D. Gale, A. García, J. Junquera, P. Ordejón, D. Sánchez-Portal, *J. Phys. Condens. Matter.* **2002**, *14*, 2745.
[39] G. Román-Pérez, J. M. Soler, *Phys. Rev. Lett.* **2009**, *103*, 096102.
[40] H. J. Monkhorst, J. D. Pack, *Phys. Rev. B* **1976**, *13*, 5188.